Preparation and adsorption behavior of amino-functionalized bridged organosilicas for the removal of Ag(I) from aqueous solutions

Song Deng, Jingrong Huang, Meng Guo, Xueni Sun, Xiuxiu Ren, Jing Zhong, Rong Xu*

Jiangsu Key Laboratory of Advanced Catalytic Materials and Technology, School of Petrochemical Engineering,
Changzhou University, Changzhou 213164, Jiangsu, China, Tel. +86 510 86330358; emails: xurong@cczu.edu.cn (R. Xu),
472856880@qq.com (S. Deng), 190332569@qq.com (J. Huang), guomengcczu@163.com (M. Guo), shellysun0110@cczu.edu.cn (X. Sun),
renxiuxiu@cczu.edu.cn (X. Ren), zjwyz@cczu.edu.cn (J. Zhong)

ABSTRACT

Novel p-phenylenediamine-bridged organosilica (PPDA-BOS-T) materials were synthesized via the co-condensation reaction assisted by tetraethyl orthosilicate (TEOS). These amino-functionalized organosilicas were characterized by Fourier transform infrared spectrometer, N_2 sorption, scanning electron microscopy, and transmission electron microscopy. The addition of TEOS played a positive role in the construction of the porous network structure of the bridged organosilicas. The saturation adsorption capacity for Ag(I) of the PPDA-BOS-T could reach 82.88 mg g^{-1}. The conformity to the Freundlich model indicated multilayer adsorption with active sites. Furthermore, the adsorption was followed well by the pseudo-second-order model, and the intraparticle diffusion was proved to be the rate-limiting step during the adsorption of Ag(I). Finally, the thermodynamic parameters including the change of free energy (ΔG), enthalpy (ΔH), and entropy (ΔS) of adsorption were calculated.

Keywords: Bridged organosilicas; Adsorption; Amino-functionalization

1. Introduction

With the acceleration of industrialization, the discharge of wastewater containing heavy metal ions poses a great threat to both the environment and human health. Particularly, heavy metal ions, which cannot be biodegraded nor disintegrated, cause severe damages to human and aquatic ecosystems [1–3]. Silver (Ag) is regarded as a precious metal due to the currency and industrial value. However, a significant amount of silver dissolved in the effluents is discharged from industries, which is toxic to living organisms. Consequently, the removal of the silver from wastewater is becoming an especially important task. While seeking an effective and environmental-friendly technology to solve the problem of heavy metals contamination is a great challenge.

Several methods have been applied to the removal of heavy metal ions, such as solvent extraction [4], electrodialysis [5], ion exchange [6], and membrane filtration [7]. Compared with the above methods, adsorption is one of the most promising methods because of its great advantages in both economy and efficiency [8–10]. Various adsorbents such as lignin [11], chitosan [12], and activated carbon [13] have been used for the removal of heavy metal ions. However, some intrinsic disadvantages of these adsorbents hamper further application, such as the irregular pore size distribution, weak interactions with metal ions, and low adsorption capacity [14].

Recently, mesoporous silica materials have been extensively used for the removal of heavy metal ions from wastewater [15,16]. The presence of silanol groups (Si–OH) on the surface provides opportunities for mesoporous silicas

to fix targeted functional groups, resulting in strong binding affinities toward heavy metal ions. As an important branch of mesoporous silicas, bridged organosilicas (BOS) have attracted considerable attention because of interesting features such as high hydrothermal stability, large surface area, and adjustable surface properties [17,18]. Generally, BOS are synthesized via hydrolysis and condensation reactions of bridged organosilanes $(R'O)_3Si–R–Si(OR')_3$. The incorporation of organic bridges (R) into the silica networks provides new opportunities to finely tune the chemical–physical properties [19]. However, the introduction of long flexible bridges is easy to cause the bending of the chains and the collapse of pore structure, thereby reducing the porosity of the silica networks [20]. Yu et al. [21] and Guo et al. [22] designed high-performance organosilica membranes by the incorporation of short and rigid groups into the nonporous matrix. Compare with the initial membranes, the gas permeances of modified membranes drastically increased. Inspired by these two investigations, the tetraethyl orthosilicate (TEOS) with rigid structures was introduced into the organosilica networks to solve the problem.

In this study, mesoporous p-phenylenediamine-bridged organosilica (PPDA-BOS-T) materials were synthesized successfully via the co-condensation reaction assisted by TEOS. The addition of TEOS is expected to play a positive role in the construction of the porous network structure of the BOS. N_2 sorption, scanning electron microscopy (SEM), and transmission electron microscopy (TEM) were applied to analyze the pore structures and morphologies of the PPDA-BOS-T. The adsorption properties of these amino-functionalized BOS for Ag(I) were investigated systematically. Finally, kinetics, thermodynamics, and isotherms of the adsorption were studied in order to understand the adsorption behaviors of the innovative PPDA-BOS-T adsorbents.

2. Experimental

2.1. Chemicals

All reagents were of analytical grade. 3-glycidoxypropyltrimethoxysilane (GPTS) was purchased from Sinopharm Chemical Reagent Co., Ltd., (Shanghai, China). Ammonium fluoride (NH_4F) was purchased from Chinasun Specialty Products Co., Ltd., (Changshu, China). TEOS was purchased from Shanghai Lingfeng Chemical Reagent Co., Ltd., (Shanghai, China). Hexadecyl trimethyl ammonium bromide (CTAB) and p-Phenylenediamine (PPDA) were purchased from Aladdin Chemical Reagent Co., Ltd., (Shanghai, China). Sodium hydroxide (NaOH) was purchased from Shanghai No.4 Reagent and H.V. Chemical Co., Ltd., (Shanghai, China). Silver nitrate ($AgNO_3$) was purchased from Reagent No.1 Factory of Shanghai Chemical Reagent Co., Ltd., (Shanghai, China). Nitric acid (HNO_3) was purchased from Sinopharm Chemical Reagent Co., Ltd.

2.2. Synthesis of PPDA-BOS-T

The PPDA-BOS mesoporous materials were prepared via the hard template method, according to Fig. 1. 10.872 g of 3-GPTS and 2.487 g of PPDA were blended in 50.0 mL of ethanol in a three-necked flask. The mixture was refluxed accompanying mechanical stirring at 358 K for 12 h
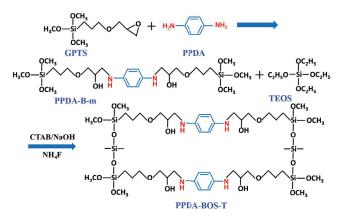

Fig. 1. Synthesis route to PPDA-BOS-T.

under nitrogen atmosphere to obtain the PPDA-bridged monomer (PPDA-B-m) ethanol solution.

0.775 g of CTAB and 0.120 g of NaOH were added to 50.0 mL of distilled water with stirring until the solid was completely dissolved into the solution. Then 0.730 g of PPDA-B-m ethanol solution and 1.160 g of TEOS were mixed and added. After stirring for 10 min, 4.0 mL of 0.014 g mL^{-1} NH_4F was added to the above solution. The reaction mixture was stirred at room temperature for 24 h. Then the mixture was transferred into Teflon-lined autoclaves and heated at 358 K for 4 d. After filtering, the product was washed with water, dried at 333 K. The solid product was collected and then solvent-extracted with ethanol and HCl for 72 h. After filtration, washing with water, and vacuum drying at 333 K, the final organosilica material was obtained and denoted as PPDA-BOS-T, where T referred to TEOS. For comparison, PPDA-BOS was prepared without TEOS.

2.3. Characterization

Fourier transform infrared spectrometer (FT-IR, Nicolet-460, USA) was applied to confirm the chemical structure of PPDA-BOS-T in the wavenumber ranging from 600 to 3,600 cm^{-1}. The samples were pressed into KBr disks. Before measurement, the sample was outgassed overnight at 393 K. Heavy metal ions in solution were measured by inductively coupled plasma atomic emission spectrometry (ICP-AES, Aglient 5110, USA). The structure and morphology of the adsorbent were examined using field-emission scanning electron microscopy (FE-SEM, Zeiss SUPRA 55, Germany) with an acceleration voltage of 5 kV. Prior to imaging, solid samples were deposited on metallic support and covered with a layer of platinum. TEM images of adsorbent were obtained using JEOL, JEM-2100 electron microscope (Japan). The solid samples were first dispersed in absolute ethyl alcohol, then deposited on a copper grid. Nitrogen adsorption–desorption isotherms of PPDA-BOS-T adsorbent were determined by nitrogen sorption at 77 K, using a volumetric adsorption analyzer (ASAP 2020, USA). The BET method was employed in a relative pressure range of $P/P_0 = 0$–1.00 to calculate the specific surface area. The pore size distribution was obtained through the analysis of the adsorption branch of nitrogen isotherms using the BJH model.

2.4. Static adsorption experiments

10.0 mg of PPDA-BOS-T adsorbents were mixed with 10.0 mL of $AgNO_3$ solution with a concentration of 100 mg L^{-1} at pH = 6 in a thermostatic shaker. The resulting mixture was shaken at 200 r min^{-1} under 288 K for 24 h to reach the final equilibrium state. The initial and final concentrations of Ag(I) were analyzed by ICP-AES. The adsorption capacity and removal efficiency can be calculated by the following equations:

$$q_e = \frac{(C_0 - C_e)V}{m} \tag{1}$$

$$R = \frac{C_0 - C_e}{C_0} \times 100\% \tag{2}$$

where C_0 (mg L^{-1}) and C_e (mg L^{-1}) are the concentration of Ag(I) at the beginning and at time t (min), respectively. q_e (mg g^{-1}) is the adsorbed amount. V (mL) represents the volume of solution, m (mg) is the dry weight of the adsorbent, and R (%) represents removal efficiency.

2.5. Adsorption isotherms

Adsorption isotherms were performed by adding 10.0 mg of PPDA-BOS-T adsorbents to 10.0 mL of Ag(I) solution with various initial concentrations. After being shaken at 288 K for 24 h, the Ag(I) concentration in the liquid phase was analyzed. Isotherm data were analyzed with Langmuir and Freundlich models.

2.6. Kinetics and thermodynamics

10.0 mg of PPDA-BOS-T adsorbents were added into 10.0 mL of $AgNO_3$ solution (100 mg L^{-1}) at pH = 6 under 288 K. The concentration of Ag(I) was analyzed at various time intervals. Based on experimental data, adsorption kinetics were simulated by pseudo-first-order, pseudo-second-order, and Webber Morris intra-particle diffusion models.

In order to investigate the adsorption mechanism of solid–liquid interface, the Langmuir model [23] and Freundlich model [24] were employed to fit the experimental data. The linear form of the Langmuir model is expressed by Eq. (3):

$$q_e = \frac{q_m C_e K_L}{K_L + C_e} \tag{3}$$

where q_e (mg g^{-1}) is adsorption capacity, and C_e (mg L^{-1}) refers to the equilibrium concentration of metal ions. q_m (mg g^{-1}) is theoretical maximum adsorption capacity, and K_L (L mg^{-1}) is the Langmuir exponent, relating to the affinity of binding sites.

The linear form of the Freundlich model is expressed by Eq. (4):

$$q_e = K_F C_e^{1/n} \tag{4}$$

where K_F (mg g^{-1}) is the binding energy constant that reflects the affinity of the adsorbents to metal ions, n represents the Freundlich exponent related to adsorption intensity.

In order to investigate the adsorption rate and kinetic mechanism of Ag(I) onto PPDA-BOS-T, pseudo-first-order [25] and pseudo-second-order [26] kinetic models were used to analyze the kinetics of the adsorption process. The pseudo-first-order and the pseudo-second-order kinetic model are expressed by Eqs. (5) and (6), respectively.

$$\ln(q_e - q_t) = \ln q_e - k_1 t \tag{5}$$

$$\frac{t}{q_t} = \frac{1}{k_2 q_e^2} + \frac{t}{q_e} \tag{6}$$

where q_e (mg g^{-1}) and q_t (mg g^{-1}) are adsorption capacity at equilibrium and time t (min), respectively, k_1 (min^{-1}) and k_2 (g mg^{-1} min^{-1}) are kinetic adsorption rate constants for the pseudo-first-order kinetic and pseudo-second-order, respectively.

Generally, the changes in thermodynamic parameters during the adsorption process could be detected by adsorption experiments at different temperatures. The thermodynamic parameters including ΔG (Gibbs free energy change), ΔS (entropy change), and ΔH (enthalpy change) could be calculated by applying the thermodynamic equations, as expressed by Eqs. (7) and (8) [27]:

$$\Delta G = -RT \ln K_C \tag{7}$$

$$\ln K_C = \frac{\Delta S}{R} - \frac{\Delta H}{RT} \tag{8}$$

where ΔG (kJ mol^{-1}) means Gibbs free energy change, ΔS (J mol^{-1} K^{-1}) means entropy change and ΔH (kJ mol^{-1}) means enthalpy change, R (8.314 J mol^{-1} K^{-1}) means gas constant, and T (K) refers to adsorption temperature. Adsorption of Ag(I) on the PPDA-BOS-T can be regarded as a reversible process, and the adsorption equilibrium constant K_C can be expressed by Eq. (9):

$$K_C = \frac{C_0 - C_e}{C_e} \tag{9}$$

$$q_t = K_{id} t^{1/2} + C \tag{10}$$

where K_{id} (mg g^{-1} min^{-1}) is the intraparticle diffusion rate constant, C (mg g^{-1}) represents the thickness of boundary layer (the higher value of C, the greater the boundary layer effects).

3. Results and discussion

3.1. FT-IR spectroscopy

FT-IR was applied to analyze the chemical structure of the PPDA-BOS-T materials. As shown in Fig. 2, the absorption bands at 1,075 and 803 cm^{-1} were attributed to the asymmetric and symmetric vibrations of Si–O–Si,

correspondingly. The saturated C–H stretching vibration was shown clearly in PPDA-BOS-T at 2,925 cm^{-1} [28]. The broad absorption peak at 1,640 cm^{-1} could be attributed to the stretching vibration of C=O. The broad absorption peak at 1,521 cm^{-1} confirmed the introduction of benzene rings into the networks [29]. The presence of stretching modes at 3,438 cm^{-1} was an indication of –OH and N–H [30].

3.2. SEM and TEM observation

Fig. 3 shows the SEM and TEM images of the PPDA-BOS and the PPDA-BOS-T adsorbents. Clearly, the surface of the PPDA-BOS adsorbent was smooth. The roughness of the surface and the visibility of pores within the PPDA-BOS-T
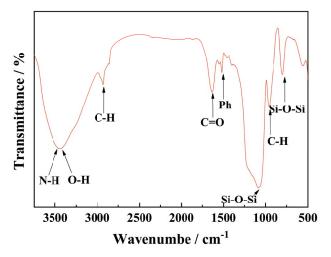
Fig. 2. FT-IR spectra of the PPDA-BOS-T.

tended to be increased with the addition of TEOS. Without the assistance of TEOS, the long organic bridges were easy to cause the bending of the chains due to their high flexibility, hence reducing the porosity of the resultant adsorbents. In addition, amino-functional groups were wrapped in a closed structure and hardly contacted with Ag(I) ions, which weakened the adsorption performance. With the introduction of TEOS, the space between the organic bridging groups was enlarged, which effectively alleviated the bending problem of the chains. TEM results were consistent with SEM analysis, where TEOS was considered to play a positive role in constructing porous silica network structure. The increase in space between the chains facilitated the entry of Ag(I) into the inside of the network channels and contact with the active functional groups, enhancing the adsorption capacity of the adsorbents.

3.3. Nitrogen adsorption–desorption isotherms

To probe the pore structure of amino-functionalized BOS, nitrogen gas sorption measurements were performed on the PPDA-BOS-T and PPDA-BOS. As presented in Fig. 4a, both of the isotherms presented type IV characteristics according to the IUPAC classification. Fig. 4b clearly revealed that the pore size distribution of PPDA-BOS-T and PPDA-BOS samples located in the mesoporous region. Detailed information on the textural properties is given in Table 1. Compared to PPDA-BOS, the pore size, and BET surface area of PPDA-BOS-T significantly increased, suggesting the successful incorporation of rigid TEOS. The PPDA-BOS-T displayed a high BET specific surface area of 461 m^2 g^{-1} and a pore volume of 1.2 cm^3 g^{-1}, which was beneficial for the adsorption capacity.
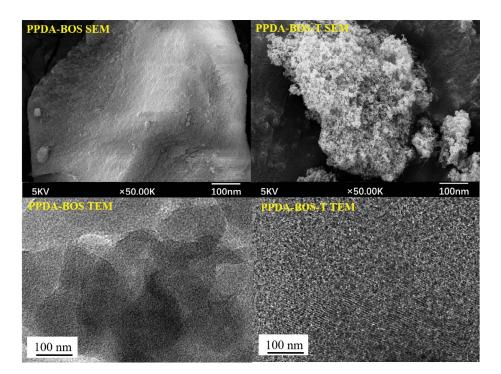
Fig. 3. SEM and TEM images of the PPDA-BOS (left) and the PPDA-BOS-T (right) adsorbents.
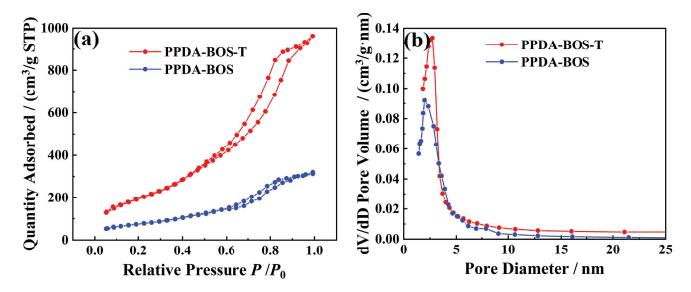
Fig. 4. Nitrogen adsorption–desorption isotherms (a) and BJH pore size distributions (b) of PPDA-BOS-T and PPDA-BOS.

Table 1
Textural properties of PPDA-BOS-T and PPDA-BOS

Adsorbents	S_{BET} (m^2 g^{-1})	V_{BJH} (cm^3 g^{-1})	D_a (nm)
PPDA-BOS	278.4	0.96	5.3
PPDA-BOS-T	461.2	1.2	8.4

3.4. Adsorption properties of PPDA-BOS-T materials

3.4.1. Effect of pH value

Fig. 5 shows the effect of pH on adsorption capacity and removal efficiency of the PPDA-BOS-T for Ag(I). Both the adsorption capacity of the PPDA-BOS-T and the removal efficiency of Ag(I) increased with an increase in pH and was achieved the maximum adsorption capacity at pH = 6. At low pH, amino groups were protonated, resulting in a decrease in active binding sites. Moreover, the electrostatic repulsion between the protonated amino groups and Ag(I) further hindered the adsorption of Ag(I) [31]. As the pH values increased gradually, the decreased protonation effect of the amino groups enhanced the adsorption capacity of the PPDA-BOS-T. However, when the pH was over 6, Ag(I) would form hydroxide precipitate. Therefore, the subsequent adsorption experiments were carried out under pH = 6.

3.4.2. Effect of Ag(I) initial concentration

Fig. 6 presents the concentration of Ag(I) on adsorption capacity and removal efficiency. The adsorption capacity of PPDA-BOS-T increased gradually as the initial concentration of Ag(I) increased. This was attributed to the increased driving force. Whereas the removal efficiency decreased with an increase in the Ag(I) concentration. At low initial concentration, the binding sites and pore volume of the adsorbent were sufficient to adsorb Ag(I), leading to a high removal efficiency. As the initial concentration
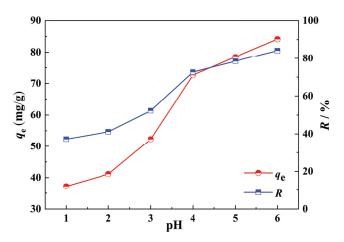

Fig. 5. Effect of pH on adsorption capacity and removal efficiency of the PPDA-BOS-T for Ag(I). m/V = 1 g L^{-1}, C_0 = 100 mg L^{-1}, and T = 288 K.
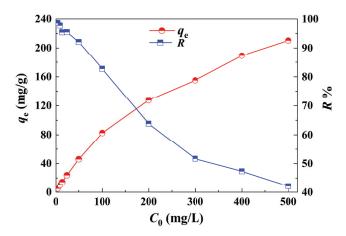

Fig. 6. Effect of Ag(I) concentration on adsorption capacity and removal efficiency for the PPDA-BOS-T. m/V = 1 g L^{-1}, pH = 6, and T = 288 K.

increased, binding sites and the pore volume reduced relatively and the competitive adsorption occurred among the Ag(I). As a result, the adsorption of Ag(I) was gradually suppressed and the removal efficiency decreased.

3.4.3. Effect of contact time and temperature

The effect of contact time on the adsorption of Ag(I) at different temperatures is shown in Fig. 7. The kinetic curve revealed that the adsorption capacity increased rapidly during the first 120 min, and then reached equilibrium gradually. The fast adsorption rate was attributed to the physical and reactive adsorption between Ag(I) ions and the amino groups which could quickly capture Ag(I). As the adsorption time increased, the active binding sites decreased, leading to a reduced adsorption rate. The subsequent slow step was due to the diffusion of Ag(I) ions into the inner of the adsorbent. As the temperature increased from 288 to 308 K, the adsorption capacity of Ag(I) gradually decreased from 82.88 to 59.74 mg g^{-1}, indicating that the reaction was exothermic in nature.

3.4.4. Adsorption isotherms

Fig. 8 presents the nonlinear fittings using the Langmuir model and Freundlich model for adsorption of Ag(I) on the PPDA-BOS-T. The kinetic parameters of models with correlation coefficients are given in Table 2. Fitting accuracy was determined by the correlation coefficient (R^2), the correlation coefficients of Langmuir model (R_L^2) and Freundlich model (R_F^2) were calculated to be 0.9695 and 0.9849, respectively. Obviously, the isothermal adsorption line of the PPDA-BOS-T for Ag(I) was more consistent with the Freundlich model. Therefore, the adsorption of Ag(I) on the PPDA-BOS-T could be described by the multilayer adsorption. Moreover, the value of n is 2.27, indicating that the adsorption intensity was favorable over the entire range of concentrations.
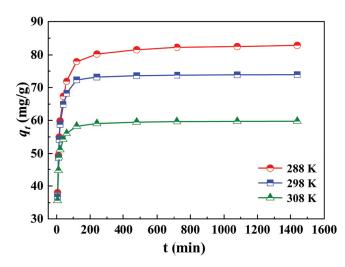
3.4.5. Adsorption kinetics

The linear fitting results with pseudo-first-order and pseudo-second-order kinetic models are shown in Fig. 9. The experimental data were fitted with the kinetic models, which are summarized in Table 3. By comparing the correlation coefficient R^2, it could be seen that the adsorption behaviors at all temperatures conformed to the pseudo-second-order kinetic model. Calculated adsorption capacity based on the pseudo-second-order kinetic model was in good agreement with the experimental results. Hence, the adsorption process followed well the pseudo-second-order model.

However, neither pseudo-first-order kinetic model nor pseudo-second-order kinetic model could determine the diffusion mechanism. The transmission of heavy metal ions from the bulk solution to the out of liquid film can be ignored in the adsorption system with severe agitation and oscillation. On this premise, three types of mechanisms are involved in the adsorption process, including film diffusion, intraparticle diffusion, and adsorption [32]. Film diffusion involves the transport of metal ions from the bulk solution to the external surface of the adsorbent, which is identified as an external mass transfer resistance. Film diffusion is followed by intraparticle diffusion, in which the adsorbed ions diffuse into the pores of adsorbents. This process is associated with intraparticle mass transfer resistance (pore-volume diffusion or surface diffusion). Adsorption is a fast step and the limit on the adsorption rate can be negligible. Therefore, the adsorption rate is limited by film diffusion and intraparticle diffusion. Weber–Morris intraparticle diffusion model assumes that the intraparticle diffusion is a rate-control step, which is expressed by Eq. (10) [33].
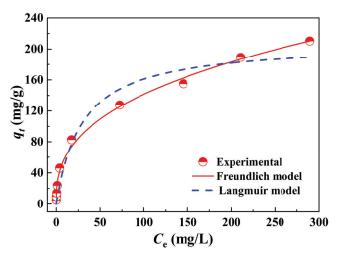

Fig. 8. Adsorption isotherms of the PPDA-BOS-T for Ag(I) with Langmuir model (dash) and Freundlich model (solid).

Table 2
Kinetic parameters of Langmuir model and Freundlich model

Model	q_m (mg g^{-1})	n	K	R^2
Langmuir	205.3	/	0.0601	0.9695
Freundlich	/	2.27	19.31	0.9849

Fig. 7. Kinetic profiles of the PPDA-BOS-T for adsorption of Ag(I) at different temperatures. m/V = 1 g L^{-1}, C_0 = 100 mg L^{-1}, and pH = 6.
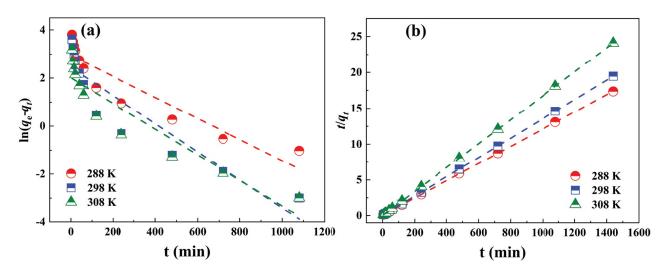
Fig. 9. (a) Pseudo-first-order and (b) pseudo-second-order model for adsorption of Ag(I) with the PPDA-BOS-T at different temperatures. $m/V = 1$ g L^{-1}, $C_0 = 100$ mg L^{-1}, and pH = 6.

Table 3
Kinetic parameters for adsorption of Ag(I) on the PPDA-BOS-T at different temperatures

T (K)	k_1 (min^{-1})	q_{e1} (mg g^{-1})	R_1^2	k_2 (g mg^{-1} min^{-1})	q_{e2} (mg g^{-1})	R_2^2
		Pseudo-first-order			Pseudo-second-order	
288	0.0044	0.0059	0.8427	0.0015	83.26	0.9993
298	0.0059	11.50	0.8330	0.0029	74.24	0.9996
308	0.0053	7.48	0.8518	0.0047	59.88	0.9992

Fig. 10 shows the linear fitting using the Weber–Morris intraparticle diffusion model for adsorption of Ag(I) with the PPDA-BOS-T. The intraparticle diffusion rate (K_{id}) and correlation coefficient were determined by calculating the straight-line plot of q_t against $t^{0.5}$. If the intraparticle diffusion kinetic model fits a straight line that passes through the origin (C=0), the whole adsorption process will be only controlled by the intraparticle diffusion. Whereas if the fitting shows a multi-linear plot, which means there are two or more steps involving in the adsorption process. As shown in Fig. 10, there are three straight lines with different slopes. The first two segments of the fitted line represented two control steps of pore volume diffusion and surface diffusion, respectively. The third fitting line indicated that adsorption had reached the dynamic equilibrium stage. During the pore volume diffusion, Ag(I) diffused to the inner surface of the adsorbent. The diffusion rate was slower than that for the pore-volume diffusion (corresponding to the slope of the second straight line), probably due to the reduction of concentration gradient and influence of flow friction resistance in surface diffusion. The dotted line represented the liquid film diffusion that was located before the intraparticle diffusion. The slope was higher than that of two intraparticle diffusion lines, indicating that its diffusion rate was higher than that of intraparticle diffusion. The intraparticle diffusion was therefore the rate-limiting step in the whole adsorption process.
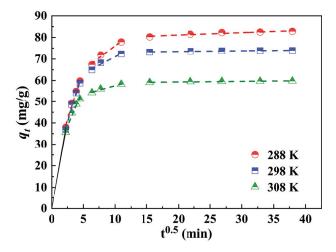

Fig. 10. Fitting of the intraparticle diffusion model for adsorption of Ag(I) with the PPDA-BOS-T.

3.4.6. Adsorption thermodynamics

As shown in Fig. 11, a linear relationship is observed clearly with the fitting of lnK_C against $1/T$.

Values of ΔS and ΔH were obtained through the calculation of the slope and intercept of the fitting line, which is summarized in Table 4.

Table 5
Comparison of some adsorbents from the reported literatures

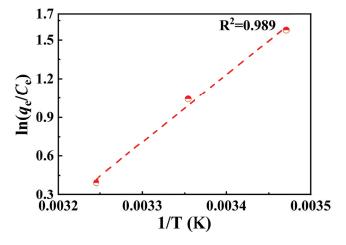| Adsorbed materials	C_0 (mg L^{-1})	T (°C)	q_e (mg g^{-1})	Ref.
Functional nano-TiO$_2$	100	25	74.5	[34]
Ag(I)-imprinted thiol-functionalized polymer	100	25	29.8	[35]
An Ag$^+$-imprinting CTS biosorbent	100	25	25	[36]
Functional poly (glycidyl methacrylate)	100	28	119.9	[37]
Chitosan/polydopamine@C@magnetic fly ash	100	30	23.8	[38]
TPCMFA	100	30	46.9	[39]
PT-GO biosorbent	100	30	272	[31]
PPDA-BOS-T	100	25	73.9	This work

Fig. 11. Van't Hoff plot for adsorption of Ag(I) with the PPDA-BOS-T.

Table 4
Thermodynamic parameters for adsorption of Ag(I) with PPDA-BOS-T

Temperature (K)	ΔH (kJ mol^{-1})	ΔS (J mol^{-1} K^{-1})	ΔG (kJ mol^{-1})
288			–3.778
298	–43.585	–137.96	–2.584
308			–1.011

The negative value of ΔG at three temperatures indicated the adsorption process was spontaneous. The absolute value of ΔG decreased as the temperature raised, indicating the adsorption of Ag(I) was easier to proceed at low temperatures. The negative value of ΔH suggested that the adsorption process was exothermic in nature. ΔS less than 0 indicated that the disordered state of the system reduced due to the combination of Ag(I) ions and adsorbent during the adsorption process.

3.4.7. Performance of PPDA-BOS-T comparison with others

The comparison of adsorption capacities of different adsorbents for Ag(I) is listed in Table 5. Compared to other adsorbents, PPDA-BOS-T exhibited a competitive adsorption capacity around 73.9 mg g^{-1} at 25°C, indicating great promise for the removal of Ag(I). Future studies will be more focused on the regeneration of the PPDA-BOS-T adsorbent.

4. Conclusion

In this study, amino-functionalized bridged organosilicas (PPDA-BOS-T) were synthesized via *in situ* co-condensation reactions with PPDA-BOS and TEOS. The introduction of TEOS in the co-condensation process would benefit the construction of porous network structure, greatly improving the porosity and surface area of these bridged organosilica materials. The prepared BOS were applied to the adsorption of Ag(I) in aqueous solutions. The adsorption fitted well with the pseudo-second-order kinetic model. The intraparticle diffusion was proved to be the rate-limiting step during the adsorption process. These innovative amino-functionalized BOS showed great promise as highly efficient adsorbents for applications in wastewater treatment containing heavy metal ions.

References

[1] Q. Xu, Y. Wang, L. Jin, Y. Wang, M. Qin, Adsorption of Cu(II), Pb(II) and Cr(VI) from aqueous solutions using black wattle tannin-immobilized nanocellulose, J. Hazard. Mater., 339 (2017) 91–99.
[2] Y. Liu, C. Luo, G. Cui, S. Yan, Synthesis of manganese dioxide/iron oxide/graphene oxide magnetic nanocomposites for hexavalent chromium removal, RSC Adv., 5 (2015) 54156–54164.
[3] Ihsanullah, A. Abbas, A.M. Al-Amer, T. Laoui, M.J. Al-Marri, M.S. Nasser, M. Khraisheh, M.A. Atieh, Heavy metal removal from aqueous solution by advanced carbon nanotubes: critical review of adsorption applications, Sep. Purif. Technol., 157 (2016) 141–161.
[4] R. Leyma, S. Platzer, F. Jirsa, W. Kandioller, R. Krachler, B.K. Keppler, Novel thiosalicylate-based ionic liquids for heavy metal extractions, J. Hazard. Mater., 314 (2016) 164–171.

[5] Y. Liu, J. Chen, Z. Cai, R. Chen, Q. Sun, M. Sun, Removal of copper and nickel from municipal sludge using an improved electrokinetic process, Chem. Eng. J., 307 (2017) 1008–1016.

[6] A. Ma, A. Abushaikha, S.J. Allen, G. McKay, Ion exchange homogeneous surface diffusion modelling by binary site resin for the removal of nickel ions from wastewater in fixed beds, Chem. Eng. J., 358 (2019) 1–10.

[7] A.M. Nasir, P.S. Goh, M.S. Abdullah, B.C. Ng, A.F. Ismail, Adsorptive nanocomposite membranes for heavy metal remediation: recent progresses and challenges, Chemosphere, 232 (2019) 96–112.

[8] Y. Niu, R. Qu, C. Sun, C. Wang, H. Chen, C. Ji, Y. Zhang, X. Shao, F. Bu, Adsorption of Pb(II) from aqueous solution by silica-gel supported hyperbranched polyamidoamine dendrimers, J. Hazard. Mater., 244–245 (2013) 276–286.

[9] L.P. Lingamdinne, Y.Y. Chang, J.K. Yang, J. Singh, E.H. Choi, M. Shiratani, J.R. Koduru, P. Attri, Biogenic reductive preparation of magnetic inverse spinel iron oxide nanoparticles for the adsorption removal of heavy metals, Chem. Eng. J., 307 (2017) 74–84.

[10] H.N. Muhammad Ekramul Mahmud, A.K.O. Huq, R.b. Yahya, The removal of heavy metal ions from wastewater/aqueous solution using polypyrrole-based adsorbents: a review, RSC Adv., 6 (2016) 14778–14791.

[11] L. Yang, H.Z. Yan, Modification of reed alkali lignin to adsorption of heavy metals, Adv. Mater. Res., 622-623 (2013) 1646-1650.

[12] M.M. Zhang, Y.G. Liu, T.T. Li, W.H. Xu, B.H. Zheng, X.F. Tan, H. Wang, Y.M. Guo, F.Y. Guo, S.F. Wang, Chitosan modification of magnetic biochar produced from *Eichhornia crassipes* for enhanced sorption of Cr(VI) from aqueous solution, RSC Adv., 5 (2015) 46955–46964.

[13] H. Yanagisawa, Y. Matsumoto, M. Machida, Adsorption of Zn(II) and Cd(II) ions onto magnesium and activated carbon composite in aqueous solution, Appl. Surf. Sci., 256 (2010) 1619–1623.

[14] E. Da'na, Adsorption of heavy metals on functionalized-mesoporous silica: a review, Microporous Mesoporous Mater., 247 (2017) 145–157.

[15] S. Ravi, Y.R. Lee, K. Yu, J.W. Ahn, W.S. Ahn, Benzene triamido-tetraphosphonic acid immobilized on mesoporous silica for adsorption of Nd^{3+} ions in aqueous solution, Microporous Mesoporous Mater., 258 (2018) 62–71.

[16] E.Y. Jeong, M.B. Ansari, Y.H. Mo, S.E. Park, Removal of Cu(II) from water by tetrakis(4-carboxyphenyl) porphyrin-functionalized mesoporous silica, J. Hazard. Mater., 185 (2011) 1311–1317.

[17] A. Thomas, Functional materials: from hard to soft porous frameworks, Angew. Chem. Int. Ed., 49 (2010) 8328–8344.

[18] R. Xu, S.M. Ibrahim, M. Kanezashi, T. Yoshioka, K. Ito, J. Ohshita, T. Tsuru, New insights into the microstructure-separation properties of organosilica membranes with ethane, ethylene, and acetylene bridges, ACS Appl. Mater. Interfaces, 6 (2014) 9357–9364.

[19] P. Van Der Voort, D. Esquivel, E. De Canck, F. Goethals, I. Van Driessche, F.J. Romero-Salguero, Periodic mesoporous organosilicas: from simple to complex bridges; a comprehensive overview of functions, morphologies and applications, Chem. Soc. Rev., 42 (2013) 3913–3955.

[20] R. Xu, P. Lin, Q. Zhang, J. Zhong, T. Tsuru, Development of ethenylene-bridged organosilica membranes for desalination applications, Ind. Eng. Chem. Res., 55 (2016) 2183–2190.

[21] L. Yu, M. Kanezashi, H. Nagasawa, M. Guo, N. Moriyama, K. Ito, T. Tsuru, Tailoring ultramicroporosity to maximize CO_2 transport within pyrimidine-bridged organosilica membranes, ACS Appl. Mater. Interfaces, 11 (2019) 7164–7173.

[22] M. Guo, M. Kanezashi, H. Nagasawa, L. Yu, J. Ohshita, T. Tsuru, Amino-decorated organosilica membranes for highly permeable CO_2 capture, J. Membr. Sci., 611 (2020) 118328, doi: 10.1016/j.memsci.2020.118328.

[23] Lalchhingpuii, D. Tiwari, Lalhmunsiama, S.M. Lee, Chitosan templated synthesis of mesoporous silica and its application in the treatment of aqueous solutions contaminated with cadmium(II) and lead(II), Chem. Eng. J., 328 (2017) 434–444.

[24] H. Yang, R. Xu, X. Xue, F. Li, G. Li, Hybrid surfactant-templated mesoporous silica formed in ethanol and its application for heavy metal removal, J. Hazard. Mater., 152 (2008) 690–698.

[25] A. Shahbazi, H. Younesi, A. Badiei, Functionalized SBA-15 mesoporous silica by melamine-based dendrimer amines for adsorptive characteristics of Pb(II), Cu(II) and Cd(II) heavy metal ions in batch and fixed bed column, Chem. Eng. J., 168 (2011) 505–518.

[26] X. Lu, Q. Yin, Z. Xin, Z. Zhang, Powerful adsorption of silver(I) onto thiol-functionalized polysilsesquioxane microspheres, Chem. Eng. Sci., 65 (2010) 6471–6477.

[27] T. Sheela, Y.A. Nayaka, Kinetics and thermodynamics of cadmium and lead ions adsorption on NiO nanoparticles, Chem. Eng. J., 191 (2012) 123–131.

[28] R. Xu, Q. Liu, X. Ren, P. Lin, J. Zhong, Tuning the pore structures of organosilica membranes for enhanced desalination performance via the control of calcination temperatures, Membranes, 10 (2020) 392, doi: 10.3390/membranes10120392.

[29] E. Mäkilä, L.M. Bimbo, M. Kaasalainen, B. Herranz, A.J. Airaksinen, M. Heinonen, E. Kukk, J. Hirvonen, H.A. Santos, J. Salonen, Amine modification of thermally carbonized porous silicon with silane coupling chemistry, Langmuir, 28 (2012) 14045–14054.

[30] J. Mosa, A. Durán, M. Aparicio, Sulfonic acid-functionalized hybrid organic–inorganic proton exchange membranes synthesized by sol–gel using 3-mercaptopropyl trimethoxysilane (MPTMS), J. Power Sources, 297 (2015) 208–216.

[31] Z. Wang, X. Li, H. Liang, J. Ning, Z. Zhou, G. Li, Equilibrium, kinetics and mechanism of Au^{3+}, Pd^{2+} and Ag^+ ions adsorption from aqueous solutions by graphene oxide functionalized persimmon tannin, Mater. Sci. Eng., C, 79 (2017) 227–236.

[32] Y.M. Hao, C. Man, Z.B. Hu, Effective removal of Cu(II) ions from aqueous solution by amino-functionalized magnetic nanoparticles, J. Hazard. Mater., 184 (2010) 392–399.

[33] S. Vasiliu, I. Bunia, S. Racovita, V. Neagu, Adsorption of cefotaxime sodium salt on polymer coated ion exchange resin microparticles: kinetics, equilibrium and thermodynamic studies, Carbohydr. Polym., 85 (2011) 376–387.

[34] N. Pourreza, S. Rastegarzadeh, A. Larki, Nano-TiO_2 modified with 2-mercaptobenzimidazole as an efficient adsorbent for removal of Ag(I) from aqueous solutions, J. Ind. Eng. Chem., 20 (2014) 127–132.

[35] X. Yin, J. Long, Y. Xi, X. Luo, Recovery of silver from wastewater using a new magnetic photocatalytic ion-imprinted polymer, ACS Sustainable Chem. Eng., 5 (2017) 2090–2097.

[36] H. Huo, H. Su, T. Tan, Adsorption of Ag^+ by a surface molecular-imprinted biosorbent, Chem. Eng. J., 150 (2009) 139–144.

[37] S. Çoruh, G. Şenel, O.N. Ergun, A comparison of the properties of natural clinoptilolites and their ion-exchange capacities for silver removal, J. Hazard. Mater., 180 (2010) 486–492.

[38] C. Mu, L. Zhang, X. Zhang, L. Zhong, Y. Li, Selective adsorption of Ag(I) from aqueous solutions using Chitosan/polydopamine@C@magnetic fly ash adsorbent beads, J. Hazard. Mater., 381 (2020) 120943, doi: 10.1016/j.jhazmat.2019.120943.

[39] L. Zhang, Y. Zhao, C. Mu, X. Zhang, Selective adsorption for Ag(I) from wastewater by carbon-magnetic fly ash beads modified with polydopamine and thiourea, Sustainable Chem. Pharm., 17(2020) 100287, doi: 10.1016/j.scp.2020.100287.